ARMA 18–554

Compaction- and shear-induced well deformation in Tyra: Geomechanics for impact on production

Schutjens, P.M.T.M., Fokker, P., Rai, U.B.B., Kandpal, J., Cid Alfaro, M.V., Hummel, N.D., Yuan, R., Klever, F., De Gennaro, S., Vaibav, J.
Shell Global Solutions International B.V., Rijswijk, The Netherlands
Bourgeois, F., Calvert, M., Ditlevsen, F., Hendriksen, P., Derer, C.
Mærsk Oil, a company of TOTAL, Copenhagen, Denmark
Richards, G., Price, J., Bere, A., Cain, J.
Rockfield Software, Swansea, United Kingdom

ABSTRACT: Multi-scale numerical geomechanical models for reservoir and overburden deformation in the Tyra chalk field (Denmark) were made, and calibrated by laboratory deformation tests and field data. The mechanical interaction between the compacting and deforming formation, cement and casing was 1) modeled as a function of well orientation, cement distribution, and mechanical properties, 2) followed by probabilistic analysis of the model results in well-failure risking models to gain insight in the effects of rock deformation on well failure, both in space and time, and then 3) used as input in fluid-flow models to forecast the impact of well-failure on production. The risk analysis revealed that, whilst further Tyra compaction will probably lead to more well failure, its impact on production is probably low. Our geomechanical modeling helped to reduce uncertainty in the high-cost multi-year Tyra Future field upgrade planned for the next years to support Tyra production over the next decades.

1. INTRODUCTION

1.1 Problem definition

About five meters of maximum subsidence has occurred so far in the Tyra chalk field (Denmark), significantly reducing the gap between wave crest and platform base (see Figures 1a, b). In addition, well deformations in reservoir and overburden have been measured and inferred by caliper data and hold-up-depth incidents (HUD) during logging and work-overs (Figures 1c, d). In the overburden, these have been interpreted mainly from the Upper Lark to Sele-Lista formation, 120 m to 400 m above the top reservoir at about 1950 m TVDss.

With the remaining 35% of the total depletion planned for the next decades, some 8 meters of total subsidence may occur by the end of Tyra field life (about 2042). Also, in view of the increasing reservoir compaction strains, there is concern that wells could catastrophically fail (and thus stop producing, i.e. terminally fail) as a result of the accumulated deformation and/or a possible acceleration of reservoir/overburden deformation. In the framework of the multi-year "Tyra Future" project (in which the Tyra production facilities are adapted to the subsiding sea-bed) field-wide and well-scale finite-element geomechanical models were built to 1) describe the compaction and subsidence, 2) study the mechanical effects of the compacting reservoir *and* its deforming overburden on cement and casing as function of well inclination, cement distribution, and mechanical properties of formation, cement and casing, and 3) provide input to reservoir fluid-flow simulations to assess the impact of Tyra well failure on production.

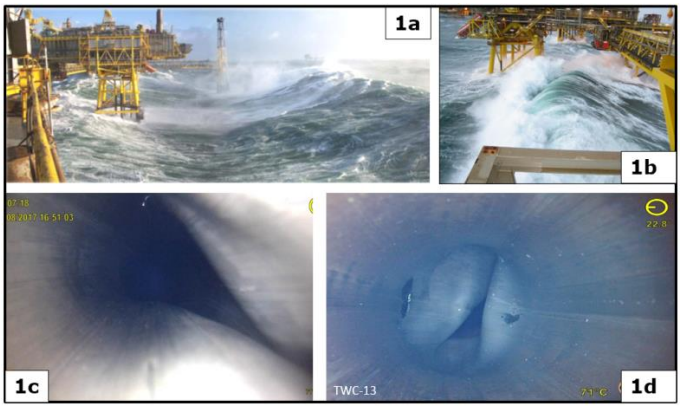

Fig. 1. Platform and breaking waves at Tyra West (1a, 1b). Casing damage in overburden observed with downhole camera (1c, 1d). Note the large reduction of the wellbore diameter, limiting production. Clearly, wireline logging and work-overs are no longer possible below the casing constriction.

1.2 Well deformation

In Tyra, there have been more than 200 HUDs and casing deformation observations that were recorded in 48 wells out of 71 wells that were logged and/or studied. 80% of these events were recorded in the high-porosity (25% to 45% bv) Lower Danian and Upper Maastrichtian chalks at the top of the reservoir. Analyzing HUD over time reveals that some restrictions of casing inner diameter occur gradually over a period of years, while others occur over a period of just a few months. Some HUDs occur in the same well, at progressively shallower depths as a function of time.

Casing and tubing deformation of wells and subsidence are caused by depletion-induced compaction, which can be several percent in high-porosity reservoirs of poorly-consolidated rock like the chalks in Tyra, Ekofisk and Valhall, and many mechanism-based/general and case-study papers are available (see Vudovich et al., 1989, De Silva et al., 1990, Teufel et al., 1991, Kristiansen et al., 2000, Nagel, 2001 and Zoback and Zincke, 2002, Dudley et al., 2005, Peng et al., 2007, and Khalmanova et al., 2008). In the literature, casing deformation simulations reveal that vertical strain less than 1% is relatively mild, in that it will probably not affect the casing integrity or well productivity (Bruno, 2002). Strains between 1% and 3% are considered transitional in terms of failure risk, while strains of 3% to 5% carry a medium-to-high risk of catastrophic (production-stopping) well deformation (Bruno, 1992; Chernocky and Scholibo 1995; Abou-Sayed et al., 2003; Li et al., 2003, Furui et al., 2009). This 3% to 5% range covers a wide spectrum of mechanical properties of the formation and cement, cement distribution, steel grade, and orientation of the well with respect to structural geology.

A further learning from the literature is that buckling and wrinkling risk is much higher for a vertical well than for an inclined well. High-angle wells (> 60 degrees) can often sustain more pressure drawdown (and thus more compaction) because they "carry" less axial strain (i.e. less shortening along the cylindrical axis of the well) and can better accommodate formation strains by bending. Next to buckling and bending, the most common and critical casing-damage mechanism identified in almost all high-compaction fields involves casing shear. This is reported to occur in the reservoir as well as in the deep overburden. The driving forces for this casing shear mechanism are the reservoir-compaction-induced strain and stress changes, but the location of shear is also controlled by the geology, e.g. lithology boundaries, and faults and fractures (Dusseault, 2001, Yuan et al., 2018). These "planes of weakness" have a high slip tendency in formations with a high shear strain. In the reservoir, the slip tendency is exacerbated in case of high pore pressure and total stress reduction, which may result in lower values of effective normal stress on potential slip surfaces. The shear-slip tendency can increase or decrease with depletion, and typically increases during a fluid-injection-induced increase in pore pressure.

Depletion-induced reservoir compaction deforms the ***overburden*** as well. Whilst overburden extensional strains are typically very small (micro-strains), shear slip can be substantial, and slip of several centimeters can damage wells. This may pose a risk to production rates and ultimate recovery. Whilst reservoir-compaction-induced well deformation in the reservoir is well-studied, its effect on well deformation in the overburden is less clear. In the deep overburden of Tyra, at the level of the Lark formation, 12 casing deformations have been inferred from HUD and caliper data. The actual amount is probably higher, as not all wells were logged. Despite the fact that no well failure had led to loss of production, because of the very high accumulated reservoir compaction (inferred from the subsidence bowl), there is concern if overburden well deformation could increase over time, both in magnitude and extent. This would be quite serious. Hence, while deformation of casing in the reservoir often allows for some production from above the deformed zone, catastrophic well failure in the overburden would completely shut-off the access to the reservoir, and thus stop the production from that well.

1.3 Structure

This paper describes the geomechanical model set-up (section 2) and some model results on reservoir compaction and overburden deformation (3.1 and 3.2), focusing on its effect on well integrity in reservoir and in overburden (3.3 and 3.4). We then show how the geomechanical model results were used to determine the risk of well failure in Tyra in reservoir (4.1) and overburden (4.2), and how this risk analysis was implemented in models forecasting production (4.3). The conclusions are listed in section 5.

2. MODEL CONSTRUCTION

2.1. Mechanisms and constitutive model for reservoir compaction and overburden deformation

There are no reliable in-situ strain measurements in Tyra, but laboratory deformation experiments on core samples from the Tyra chalk and similar chalks from other North Sea fields indicate a highly non-linear deformation in response to pore pressure depletion. High-porosity (> 35% bv) chalks typically show a marked increase in uniaxial-strain bulk-volume compressibility (C_m) after just a few MPa of depletion ("pore collapse"). The onset of pore collapse mainly depends on 1) the depletion-induced effective stress increase, 2) the in-situ pre-production porosity, 3) the rock microstructure (inter-granular vs vuggy porosity) and 4) pore fluid composition (Rhett et al. 1998, Omdal

et al. 2010, Keszthelyi et al. 2016). The increase in C_m due to pore collapse can be two orders of magnitude, and in some experiments a factor of 200 increase in C_m has been observed during pore collapse (Figure 2a).

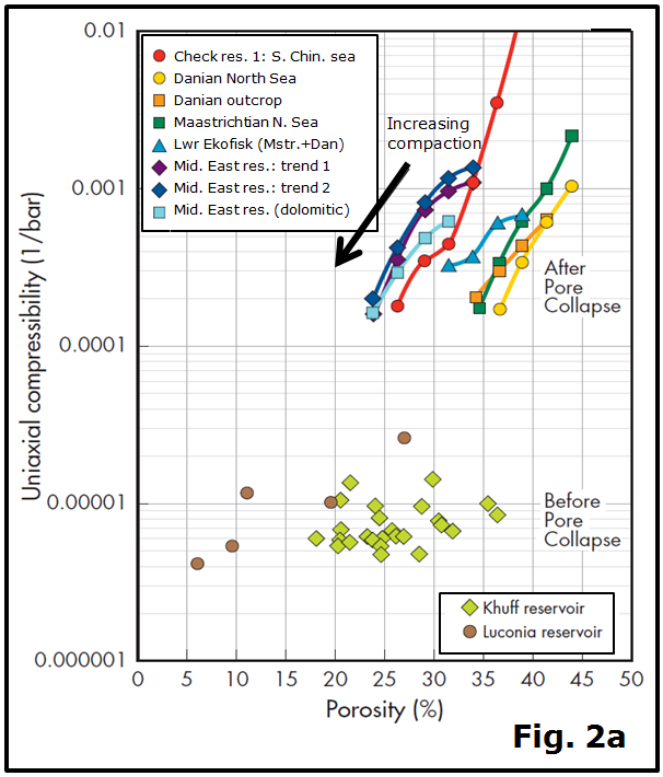

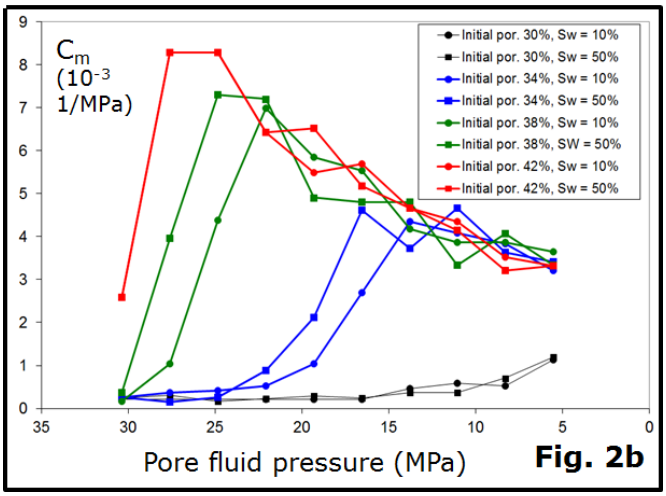

Fig. 2(a,b). Compilation of uniaxial-strain bulk-volume compressibility (C_m) as a function of porosity (Figure 2a) and pore fluid pressure (Fig. 2b, depletion increases to the right). Figure 2b is based on experimental data from Tyra. S_w is water saturation. Note the strong increase in C_m during the pore collapse stage (up to one order of magnitude), followed by the gradual non-linear decrease in C_m as depletion continues

Typically, the higher the porosity of the chalk, the smaller the depletion before pore collapse starts, and the stronger the pore collapse effect in terms of strain magnitude, porosity reduction and stress path effect. Regarding the latter, the pore collapse mechanism essentially turns a friable rock, with grains cemented in place over geologic times (albeit often weak), into a largely unconsolidated rock where most grains start to move relative to one another. In doing so, the static Poisson's ratio can increase drastically. In a uniaxial-strain deformation test, this is manifested by a stronger increase in effective radial stress per unit increase in effective axial stress than before pore collapse.

Micro-mechanically, the strong C_m-increase during pore collapse coincides with an abrupt and pervasive (sample-wide) reduction in the load-bearing grain-to-grain contact area per unit volume, which triggers the time-independent inelastic strain (plasticity) and often time-dependent inelastic strain as well. Because of the zero-radial-strain boundary condition that is often applied in laboratory deformation tests, samples that undergo pore collapse do not fail via sample-size shear failure, but undergo pervasive (i.e. sample-wide) ductile cataclasis via grain rotation and grain sliding, enabled by grain breakage or grain-contact/cement breakage. As the sample undergoes the large porosity reduction by this grain-scale brittle shear deformation, with ongoing depletion, the grain-to-grain contact area per unit volume increases again, and the sample gradually stiffens and the C_m decreases. This mechanism is called "compaction hardening", see Fig. 2. Note that, in high-porosity rock, this hardening-part of the overall compaction can span most (70% to 80%) of the total depletion, compared to the shorter depletion-range (20% to 30%) for pore collapse.

In the finite-element geomechanical model for Tyra (see below), the constitutive model for the chalk reservoir rock was a Cam Clay model, based on core deformation experiments which included compaction weakening due to grain breakage and grain rotation/sliding, followed by compaction hardening (data as in Figure 2). The laboratory measurements were also used to define porosity-stiffness correlations, so that the porosity distribution from the Tyra static reservoir model could be used to define laterally (and vertically) variation in elastic stiffness and pore collapse parameters for the reservoir layers in the model.

Core deformation experiments on core samples produced a wealth of information on chalk compaction behavior in the reservoir However, other input parameters in the Tyra geomechanical model are not known or can only be poorly constrained, notably the pre-production in-situ stress state (so two scenarios were used, see Table 1), the mechanical rock properties in the overburden (see Table 2), and the frictional properties of the faults.

The non-depleting formations in the GEOMEC model were included as homogeneous and linear-elastic layers (other than the faults crossing them, see below). The poro-elastic parameters were interpreted from laboratory data and sonic log data, applying proprietary dynamic-to-static moduli conversions. The rock properties from

the Upper and Lower Lark formations in Tyra, where several of the recent overburden well deformations occurred, were reviewed using log data and results from laboratory experiments on plugs from a nearby exploration well. Their statistical distributions were determined in terms of arithmetic means and standard deviations. For the Young's modulus, the analysis resulted in relatively low mean values of 1 GPa to 1.5 GPa in seven of the 10 overburden formations, see Table 2. The other log-based rock properties were calculated in the same way. The upper-bound Poisson's ratio was limited to 0.40, and undrained conditions were assumed for the overburden rocks.

The faults in the model have a residual cohesion of 1 MPa and friction angle of 20° in the base case. This is seen as a conservative estimate of a non-cemented fault with some fault gouge or clay smear to reduce the friction angle compared to the host rock (in the range 25°-35°).

Table 1: Two models for Tyra pre-production in-situ stress

Stress model	Pore pressure (kPa/m)	S_v (kPa/m)	S_H (kPa/m)	S_h (kPa/m)
1	14.5	22.5	21.1	20.5
2	14.5	22.5	18.2	17.3

Table 2: Static rock mechanical parameters Tyra overburden

Static rock mechanical parameters in overburden			
	Formation	Static Young's modulus (GPa)	Static Poisson's ratio (-)
1	Nordland shales	1.1	0.35
2	Overpressured shale	1.5	0.35
3	Upper Lark	1.2	0.36
4	Intra Lark	1.3	0.33
5	Lower Lark	1.0	0.33
6	Horda	1.5	0.33
7	Reef	15	0.35
8	Sele/Lista C-marker	1.5	0.35
9	Ekofisk	7.7	0.24
10	Tor	8.2	0.24

2.2. Finite-element models

A 3D full-field geomechanical finite-element model was built with Shell-tool GEOMEC with dimensions of 20 x 15 x 3 km, as well as sector models to study the detailed interaction between reservoir and overburden deformation and the Tyra wells (Figure 3).

For the **full-field model**, formation tops were taken from the static reservoir model, and the overburden formation tops from the latest seismic interpretation. In the overburden, a mechanically-stiff reef structure was included (see Table 2, formation 7) as it was considered as a potential catalyst for well deformation. 20 geologic faults were included as explicit slip surfaces, most of these in the overburden[1]. Stresses and strains calculated in the GEOMEC field-scale model were used as boundary stress/strain-conditions in the sector models for well-scale deformation, see Figures 3b and 3e.

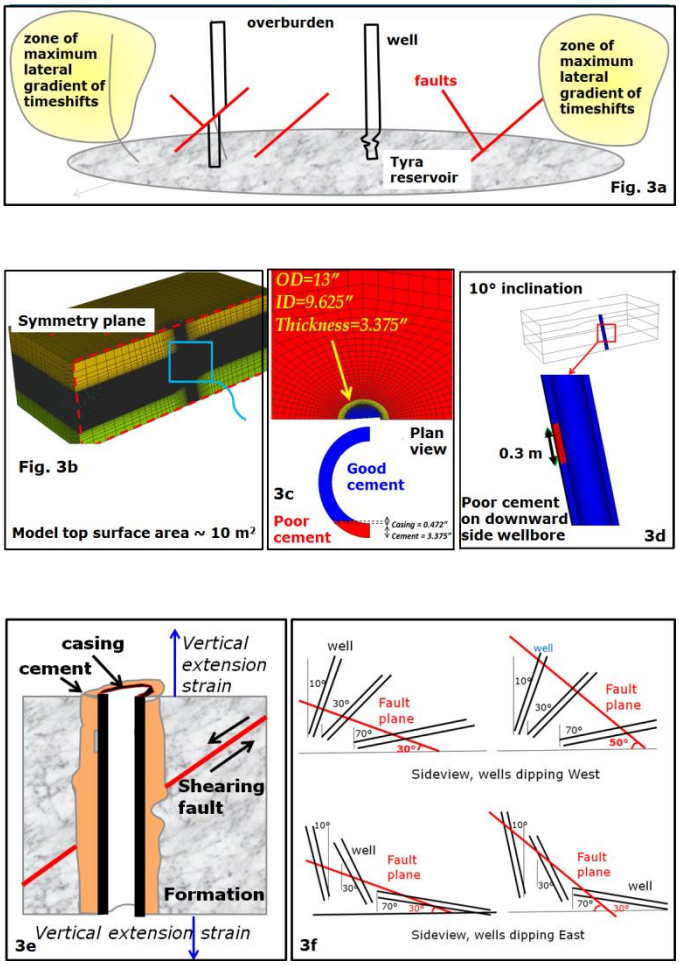

Fig. 3. Geomechanical analysis of Tyra at three scales: Field-scale of tens of kilometers (Figure 2a), with 500000 tetrahedral elements (cells), and well scale with detail of 10s to of meters. Figs 3b,c,d: casing deformation model in reservoir. Figs 3e,f: casing deformation model for overburden.

The **well-scale model for the reservoir** comprises 3D along-strike half-symmetry domains of casing, cement and chalk formation materials. The assessment was undertaken within a one (1) meter long (axial) central zone of interest with consistent size and mesh discretization, irrespective of well inclination. A Tyra-typical 9 5/8" (24.5 cm) outer-diameter casing size was

[1] The meso-scale intensive polygonal faulting in the deep overburden of Tyra was investigated by Yuan et al., 2018.

modelled. Representative well inclinations of 10°, 45° and 80° from vertical were investigated.

The constitutive model describing chalk deformation behaviour in the reservoir well scale models was Rockfield's SR3R, rate-dependent elasto-plastic with water weakening model (Crook et al., 2008), calibrated to the mechanical properties in the Tyra legacy geomechanical model and the Shell GEOMEC model. The cement was modeled with Rockfield's SR3, rate-independent elasto-plastic constitutive model, calibrated based on Shell tri-axial results on cement plugs.

Three types of casing cementation were applied in the reservoir well-scale models:

1) Good-quality cement completely surrounding the casing; 6.7 cm thick, as described above;
2) Partial-cement case: good-quality cement but with (reservoir-chalk-filled) voids on the downward side of the wellbore, i.e. patchy, see Figure 3c,d
3) Poor-quality "weak" cement, which has the same mechanical properties as the high porosity chalk.

The casing steel (thickness 2 cm) was modelled with average values for L80-grade steel, assuming that the chrome version of casing has a negligible effect on the casing deformation. (The number 80 stands for the plastic limit of the steel at 80 kpsi (about 550 MPa)). Note that the actual in-situ steel behavior can be different, since L80 is only a minimum standard, and dependent on manufacturer. The reservoir well-scale models included a casing collar, with double the stiffness and yield strength as the casing itself.

Prior to running the well-scale simulations, casing-only modeling was undertaken to verify four potential failure modes; collapse, pinch loading, bending and wrinkling, see Figure 4 for the example of wrinkling. Four elements through thickness was found to be a suitable resolution to adequately capture these deformation mechanisms.

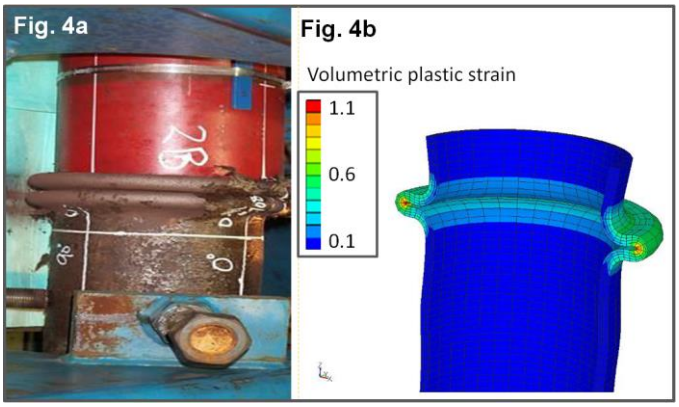

Fig. 4. Axi-symmetric wrinkling for L80 casing (Figure 4a) and model result for similar material properties and loading configuration (Figure 4b). Our well-scale model was fine-tuned with such test simulations.

Uniaxial vertical strain on the casing was imposed via displacement applied to the top surface of the domain. A vertical compaction strain of 0.15 (15% shortening) was applied, corresponding to the expected maximum depletion-induced reservoir compaction at the end of field life, based on the Tyra field-wide geomechanical model.

The **overburden well-scale models** comprised a 3D, full symmetry domain of casing, cement and overburden (Lark) formation materials; the ~200 m^3 formation block was bisected by a discrete, dipping fault plane to form a footwall and hanging wall (see Fig. 3e). The mesh comprised ~3 million tetrahedral elements, with fine elements concentrated on the casing in the area of interest, grading away towards outer domain boundaries.

Representative well inclinations of 10°, 30° and 70° were investigated, dipping West or East, and crossing the fault whose normal to the fault plane made an angle of 30° and 50° with the vertical, see Figure 3f. The intersection angle between fault and well ranged from 10° to 170°, in steps of 20°. The constitutive model describing chalk deformation behaviour in the overburden well scale models was again Rockfield's SR3 elasto-plastic model, calibrated to the mechanical properties in the Shell GEOMEC models for the Lark formation, where most of the HUDs and caliper deviation-from-circular observations were made. Cement and casing properties were the same as in the well-scale reservoir model.

Two types of casing cementation were applied in the overburden well-scale models:

1) Good-quality cement completely surrounding the casing; as described above;
3) Poor-quality "weak" cement, which has the same mechanical properties as high-porosity Tyra chalk.

Fault slip is imposed on all outer boundary surfaces of the hanging wall via an applied displacement. The foot wall outer boundary surfaces remain fully fixed. The entire interior of the model is free to deform. Interfaces between the casing-cement and cement-rock are assumed to be fully bonded (i.e. no actual frictional slip).

3. MODEL RESULTS: DEPLETION-INDUCED COMPACTION AND OVERBURDEN DEFORMATION

3.1. Field scale: reservoir

The Tyra platform subsidence as a function of time (measured by GPS) was accurately described by the model, and the calculated subsidence bowl corresponded to the measured subsidence bowl (with bathymetric

survey) to within 20%. The model indicates that the compressive strain in the Tyra reservoir is 5% to 10% in 2016, and may increase to 10% to 12%, and locally even 15% at end of field life.

3.2. Field scale: overburden

Two time-steps were analyzed: from start of production in 1984 to Jan. 2016 (Step 1) and from Jan. 2016 to end of field life, around the year 2042 (Step 2). In contrast to the very high compaction strains and the large deformation in the Tyra reservoir, the deformation in the overburden is small for Step 1 and very small for Step 2: micro-strains to tenths of micro-strain, mm's to cm's of slip, and negligible to a few MPa of total stress change. The Tyra deformation and stress change in Step 1 was much larger (10s of percent up to several factors) than in Step 2. For example, the Shear Capacity Utilization (SCU) factor, which is a measure of tendency for shear failure (see Fig. 5) increased in the Lark overburden formation by up to 13% during Step 1 as a result of the production-induced stress changes. In contrast, the SCU increased there by only up to 3% during Step 2.

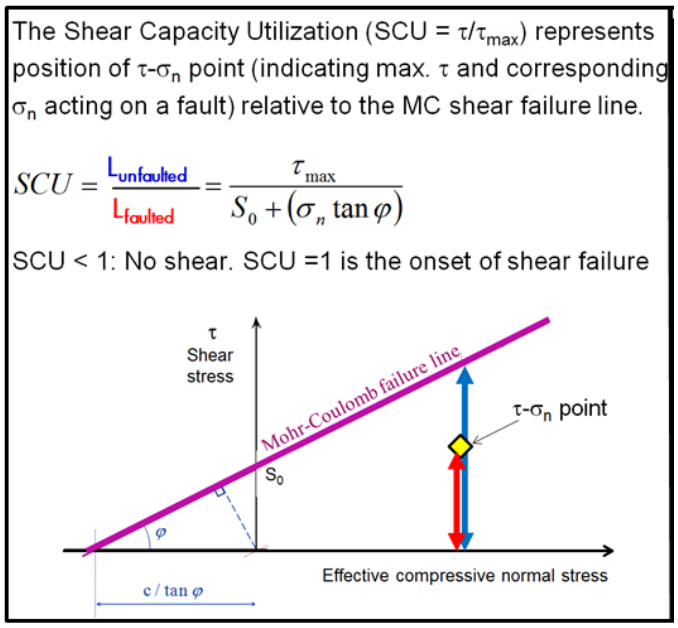

Fig. 5. Shear Capacity Utilization (SCU) parameter to quantify risk of shear failure. SCU is between 0 (no risk) and 1 (rock is at shear failure). For fault planes, a point (yellow rhomb) characterizing average stress state on fault plane is used. For the rock between the faults, the position of a Mohr *circle* is compared to the Mohr Coulomb shear failure line.

The GEOMEC model results confirm the observations by Calvert et al., 2018 and Bourgeois et al., 2018, that the Von Mises shear strain in the deep overburden of Tyra (at Lower Lark level) forms a large donut-shaped feature over the edges of the Tyra Main field (Figure 6a), coinciding with zones where there is a maximum lateral gradient in the seismic time-shifts (Calvert et al., 2018). This points to gradients in vertical extensional strain or in shear strain in the overburden. In our model, this "Von-Mises donut" grows outwards as depletion continues. A similar donut-shape is visible for the Von Mises strain in the Lark at the Tyra South West field (Figure 6b).

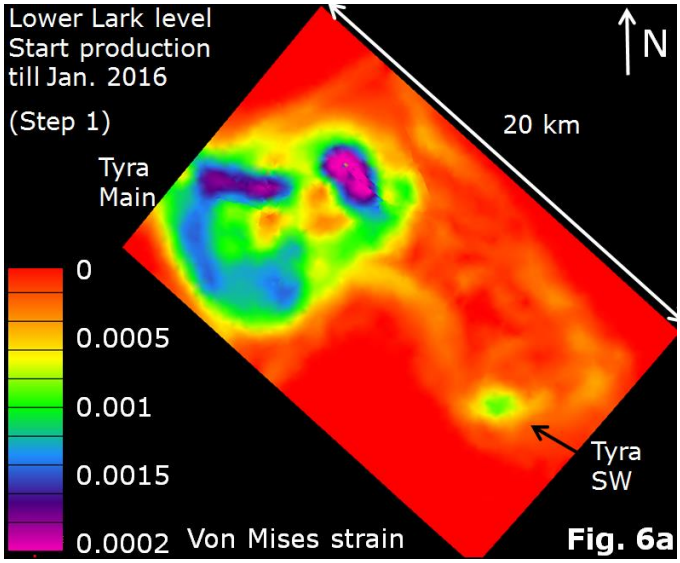

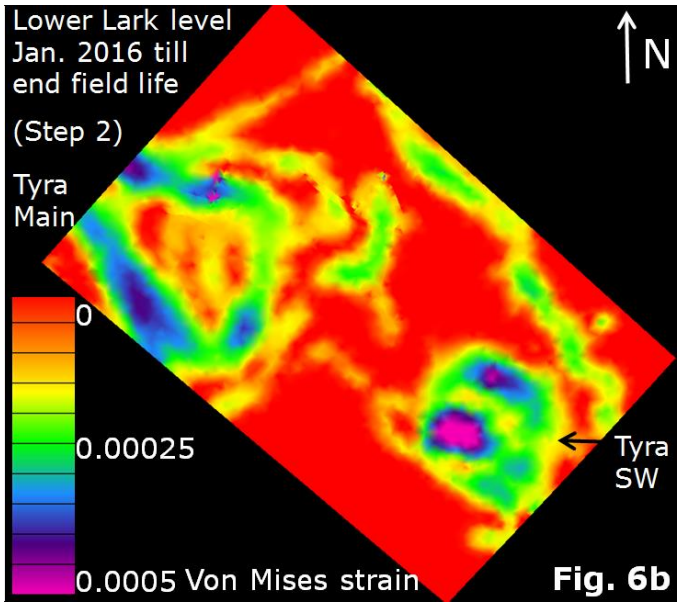

Fig. 6. Von Mises shear strain in the Lower Lark formation, from start of production till Jan. 2016 (Figure 6a) and from Jan. 2016 till the end of field life, around the year 2045 (Figure 6b). Purple colors indicate relatively high shear strain development.

The donut-feature was also seen in the stress space; - the Shear Capacity Utilization (SCU) is also donut-shaped when mapped at Lark level (Figure 7), and in a similar position as the Von Mises donut (data for Step 1).

GEOMEC shows no large changes in shear stress or effective normal stress developed in the overburden, and the 20 geologic faults in the model remain largely stable, nor did the model reveal that new shear faults formed. By the same token, no correlation was found between

GEOMEC-calculated Von Mises shear strain or SCU and the position of wells where casing constriction and HUDs were inferred.

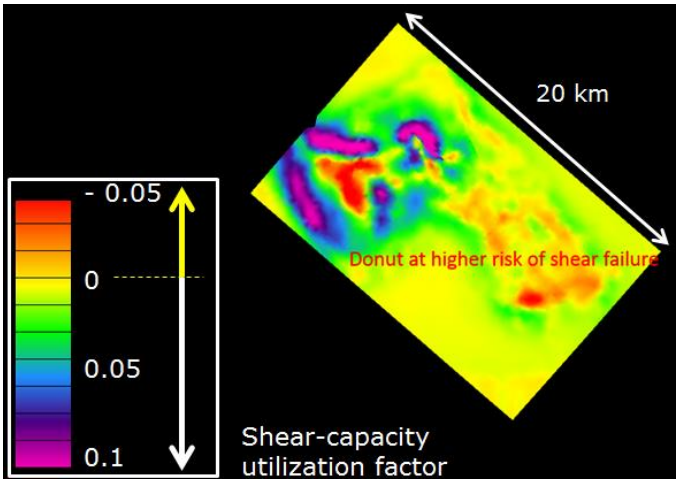

Fig. 7. SCU-change map at Lower Lark level. Note roughly circular shape ("donut") in NW part of the model. This SCU-change is between start of production and end 2016 (Step 1); warm colors mean an increase in SCU, indicating that depletion increased risk of shear failure there.

What the GEOMEC model *did* show was that most of the damaged wells in the Tyra overburden are located close to the inner side of the Von Mises and SCU donut. This was already observed by Calvert et al. (2018) based on 4D seismic data and the shear strain distribution in the Tyra legacy geomechanical model.

In some parts of the center of the Tyra overburden, virtually no deformation occurred in Steps 1 and 2 (i.e. a "passive overburden") In contrast, a local increase in shear stress and shear strain is observed in the deep overburden near the edge of the reservoir, near the stiff reef, and close to the faults. For some combinations of pre-production stress state and fault-slip properties, several cm's of fault slip was observed in the model along shear faults, in particular in the Lark formation (see Yuan et al. 2018, for similar observations on the Tyra polygonal faults).

3.3. Wellbore scale: Reservoir

Formation, cement and casing strains can be very different and inhomogeneous in one and the same model. Casing strain and casing-deformation mode are controlled by cement distribution and well inclination.

Detailed observations are from the models are:

- Near vertical wells (10° inclination) are particularly susceptible to wrinkling, irrespective of cementing quality – this results from the approximately axial loading of the casing (see Figs. 8, 9)
- Near-horizontal wells (80°-inclination) are susceptible to ovalization, irrespective of cementation – approximately transverse loading of casing (Figs. 10, 11)

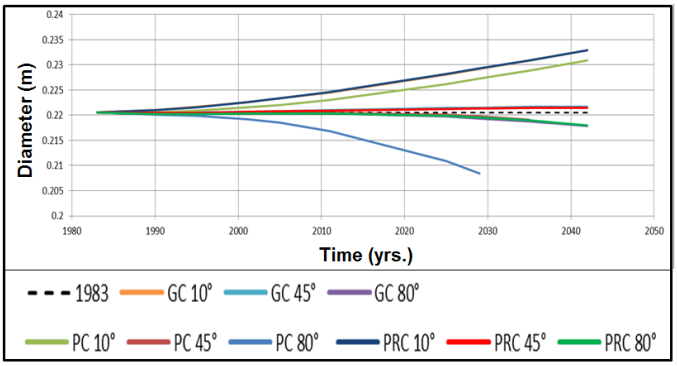

Fig. 8. Wrinkling – maximum average diameter measured along well axis through time; increase in diameter (above 0.22 m) indicative of wrinkling (as seen for the three 10° cases and 45° poor cement case). GC = good cement, PC = poor cement, PRC= partial ("patchy") cement

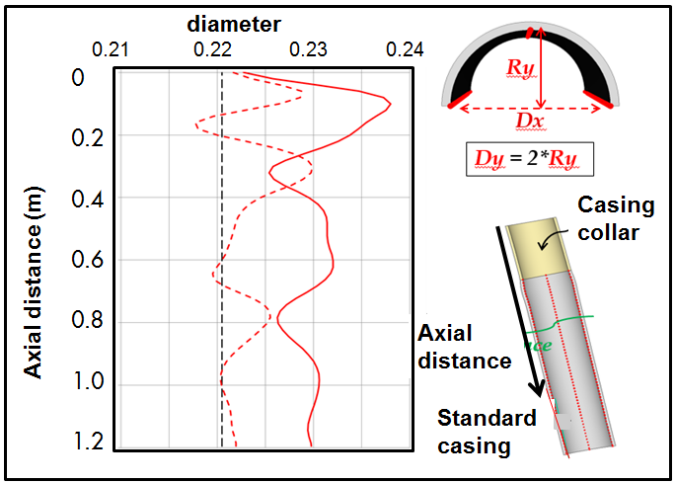

Fig. 9. Wrinkling in the 10°-inclination partial-cement case. This is the most severe wrinkling observed in the models.

- Wells inclined at 45° experience wrinkling where cementing is good / partial, and ovalization where cementing is poor
- Poor-cement cases are subject to significant shearing (Fig. 12). The absorbed load resulted in less severe casing wrinkling in the 10°-inclination poor-cement case (Fig. 8)
- Significant ovalization occurs in poor-cement 80° and 45°-cases, and is attributed to reduced lateral support offered by the shear-softened cement (Fig. 10, 12)
- The casing collar acts as an initiation point for wrinkling (Fig. 9). Poor-cement patch can act as a second initiator of wrinkling in the 10° and 45° partial cement cases, causing the most severe wrinkling (i.e. repetition of wrinkles along axis and greater lateral expansion) – Fig. 9.
- Tyra wells can undergo vertical compaction strains of 15% under any well inclination, provided the strain

field is continuous (no fault intersecting) and cementation is reasonable to good

- Wells with poor or no cementation may collapse at strains around 8% to 11%
- The model results suggest that there is no single "unique" strain that massively fails many Tyra wells.

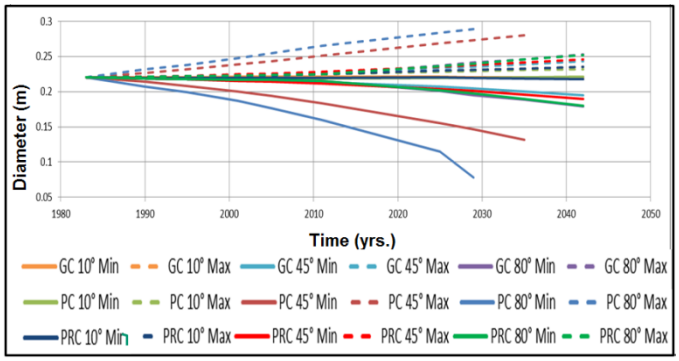

Fig. 10. Ovalization – worst case maximum and minimum diameter measured along well axis through time; deviations in diameter (above / below 0.22 m) indicative of ovalization (as seen most significantly for the 45° and 80° poor cement cases). Abbreviations are explained in Figure 8.

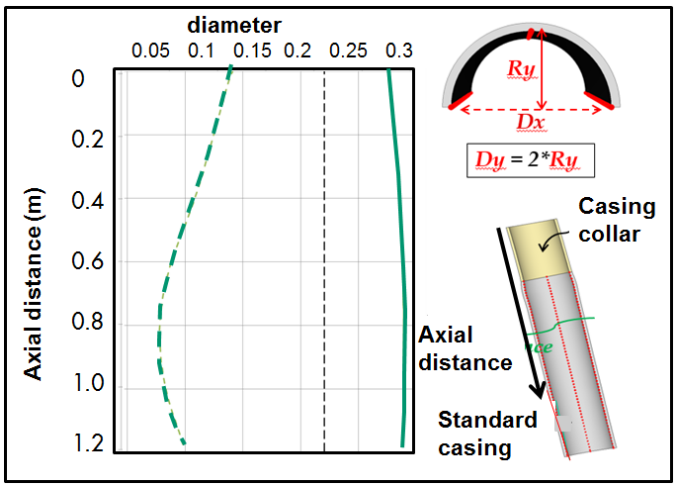

Fig. 11. Ovalization in the 80°-inclination poor-cement case. This is the most severe ovalization observed in the models.

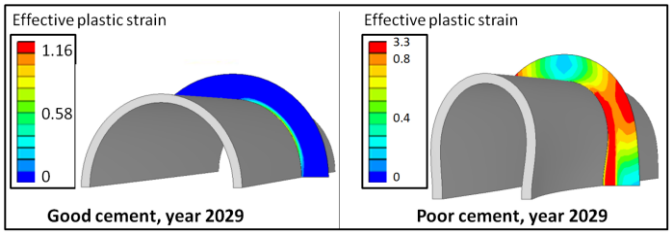

Fig. 12 Plastic strain contour shown on 2D slice through cement at center of well axis for good (left) and poor (right) cement cases; note significant shear damage within the poor cement, thereby facilitating ovalization due to reduced lateral support provided to the casing

The Appendix 1 contains observations on the calculated deformation for the chalk, cement and casing.

3.4. Wellbore scale: Overburden

Key results from the overburden well scale models are:

- Several centimeters of fault slip can indeed deform a Tyra-like casing, even if properly cemented
- For a given magnitude of fault slip, both good and poor cement results follow a bi-modal relationship between maximum casing inner-diameter (ID) change and well-fault intersection angle, and between maximum axial strain (in compression or tension) and well-fault intersection angle, see Fig. 13. Maximum values occur at well-fault intersection angles of 100° to 130°, with a smaller peak at 30° to 50°.

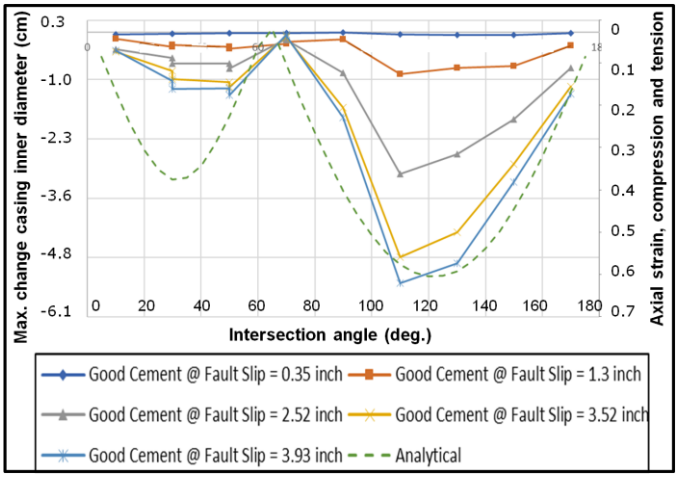

Fig. 13. Bi-modal relationship between maximum casing ID (inner-diameter) change and axial strain (on both Y-axes) and well-fault intersection angle, at increasing of fault slip. These are the model results for good cement. The results of the poor-cement simulations are similar to the good-cement ones, and to a geometry- based analytical model for casing strain (dots).

- For a given fault slip, a good-cement case records up to 40% higher maximum Von Mises plastic strain (see Appendix 2) and about 15% higher maximum casing ID reduction than its poor-cement equivalent; the greatest difference is at well-fault intersection angles of 110° to 150° (see Fig. 14).

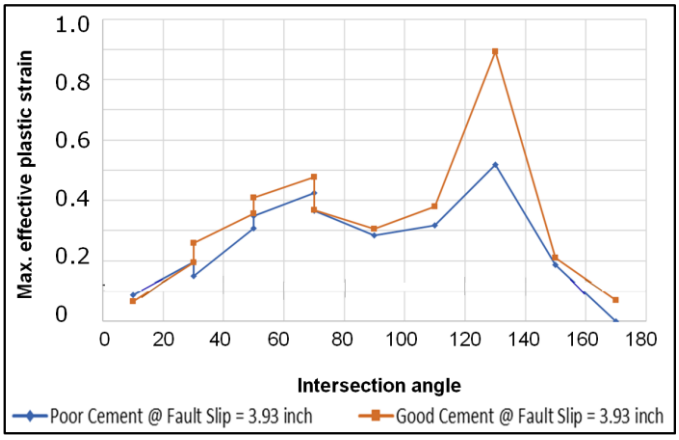

Fig. 14 Maximum Von Mises plastic strain in casing as a function of well-fault intersection angle – good vs. poor cement; dip and strike results have been combined.

Apparently, good cement results in transfer of greater load to the casing (compared to poor cement), and hence wells with good cement jobs are probably more vulnerable to shear-failure-induced damage than equivalent wells with poor cement jobs (if cut by a fault)

- For well-fault intersection angles > 90°, a casing ID increase was recorded in the strike direction, accompanied by an ID reduction in the dip direction. For intersection angles < 90°, a casing ID *increase* was calculated in the dip direction, accompanied by an ID reduction in the strike direction, see Fig. 15b,c
- For well-fault intersection angles > 90°, the largest increase in Von Mises plastic strain (equivalent to the worst damage to the casing) is recorded in the dip direction, while for intersection angles < 90° it is recorded in the strike direction
- Maximum casing ID reduction occurs at about 10 cm of fault slip ranges between negligible and ~5.6 cm
- Exceedance of the critical strain threshold – indicative of the initiation of casing rupture – is recorded at fault slip magnitudes of between ~ 4.5 cm inch and ~ 9.1 cm

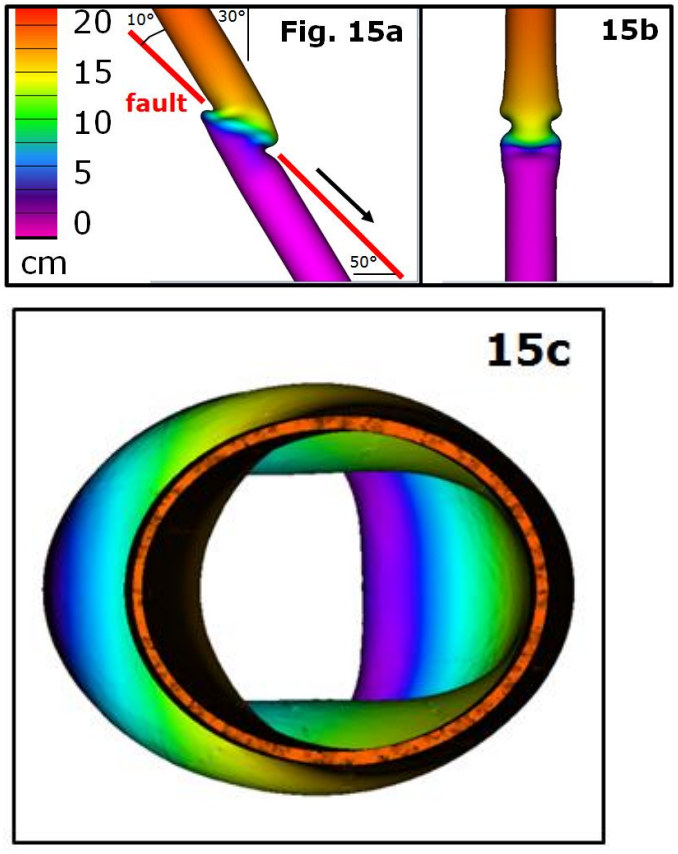

Fig. 15. Modeled shear-slip induced casing failure, with view orthogonal (Fig. 15a) and parallel (15b) to the well dip direction, and viewed along the wellbore axis (15c). This simulation has a fault dip of 50° dipping East and a well inclination of 30° dipping East, so the well-fault intersection angle is 10°.

4. FROM GEOMECHANICAL MODEL RESULT TO WELL FAILURE RISK ANALYSIS

4.1. Wells in the reservoir

Critical vertical compaction strains at which catastrophic failure of the Tyra wells occurred in the reservoir (stopping production, i.e. terminal failure) were determined from well-scale model results of nine Tyra-specific combinations of well inclination and cement distribution: inclination of 10°, 45° and 80°, and good, patchy and poor cement. Typical model results for casing deformation observed in these nine scenarios are shown in Figure 16, and are further described in the Appendix 1. The critical-strain estimate included a comparison of the Tyra-calculated compaction strains with a Shell-database for reservoir-compaction-induced casing failure in reservoirs world-wide.

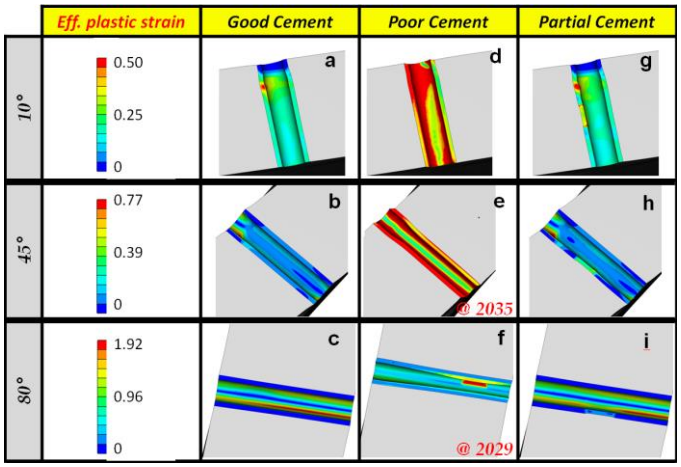

Fig. 16. Modeled plastic strain in the **steel casing** at the end of field life, year 2042. All results are for the year 2042 (end of Tyra field life), except the poor-cement 45°-inclination and poor-cement 80°-inclination well. The results from these two simulations do not go beyond the years 2035 and 2029, respectively, when the models became numerical unstable due to local casing collapse by strong ovalization.

With the prediction of critical strain at which wells of a given inclination and degree of cementation would fail in the compacting reservoir (see Figure 17), the time-at-catastrophic failure of the Tyra resource wells (selected to be the producer wells after the platform refurbishment in the Tyra Future project) could be calculated from the vertical strain in the full-field geomechanical model. To this end, the Tyra wells were grouped in nine batches according to their inclination and degree of cementation. Since the latter was not known for most wells, we assumed (after discussion with the Tyra project team) that the vertical wells have good cementation, that inclined wells are all partially cemented, and that the horizontal wells have poor cementation. Forward models of time-of-failure from the start of production were then compared with actual Tyra well failures to calibrate the well-failure risking model (Fig. 17b). In addition, a calibration factor was included by assuming a stiffer

casing for a set of Tyra wells. The calibration was fairly successful, yet a large uncertainty remained depending on how the calibration factors were combined.

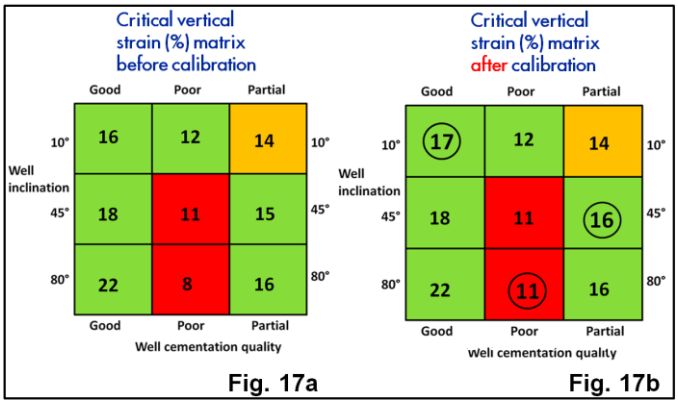

Fig.17. Matrix indicating critical vertical strain in the reservoir chalk (number in box is strain in %, so 16 means a strain of 0.16) where nine sets of Tyra wells will fail as a function of well inclination and cement quality (good meaning strong hard cement surrounding most of the casing). Figure 17a is before calibration to actual Tyra well failure data; Figure 17b is after calibration. The encircled numbers were optimized as a result of the calibration.

Our risk analysis predicted that, from the 42 resource wells in Tyra, 4 to 16 wells would fail in the reservoir as a result of compaction from 2017 till the end of field life around 2042. The large range (4 to 16) reflects the strong impact of the calibration factors and risk criteria set by the Tyra partners. Importantly, *we know where these 4 to 16 wells are*, and what their planned (forecasted) production is supposed to be. Via integration of geomechanics and reservoir engineering, we can now investigate the effect of well failure on production. This distinguishes our mechanism-based work from a purely statistical analysis, with e.g. wells picked randomly.

The 4-to-16-well-failure result was used as input in the Tyra fluid-flow model, "switching off" these wells in the fluid-flow simulation in the computer-year when the geomechanical model indicated that they would catastrophically fail. Surprisingly, the fluid-flow model results show that the impact of well failure on Tyra gas production is small: only up to 5% of the production in case all Tyra wells stay "healthy" (i.e. do not fail). Further analysis revealed that this is because 1) most wells would fail late in field life, 2) wells more likely to fail are older so there are less reserves are attached to them, 3) neighboring wells "take over" a large part of the production that the failed wells would have delivered (well interference, or "shouldering" effect). Regarding the first point, this late-in-life failure is because most reservoir rock is probably in the "compaction hardening" phase now, so the strain per unit depletion is already reducing, and so is the incremental strain on the casing per unit of time or depletion.

4.2. Wells in the overburden

The Tyra field-scale geomechanical model reveals that, even in the model with relatively high total stress anisotropy (stress model 2, see Table 1), the Tyra faults identified on seismic and the rock between the faults are not critically loaded; the risk of shear failure was low before and during production, and will increase but remain low during future production. In addition, the compaction-induced changes in total stress are very small (typically < 5% of the absolute value of the stress), and certainly not sufficient to get to Shear Capacity Utilization (SCU) values of 1. In most of the Tyra field, the overburden does not "react" to the compacting reservoir, but rather sinks along with it. So how can we explain the 12 well-deformation observations in the Tyra overburden? Quantification of shear failure risk based on a well-by-well mechanism-based analysis is of no use, since with such low SCU-values, we would predict that no well in Tyra would ever fail in the overburden.

In order to still extract maximum value from the geomechanical model results, a well-failure risking model was made indicating which Tyra wells are *relatively vulnerable* to shear-slip-induced casing damage compared to other Tyra wells. The assessment from high-risk to low-risk used the following parameters from the well-scale and the field-scale model results from Step 1 (pre-production till Jan. 2016): well-scale model results of peak rock deformation (Von Mises strain along the well-path), proximity to plasticity and shear failure (SCU), observed casing deformation (known weakened but not-yet-collapsed wells), proximity to one of the 20 large geologic faults in the 3D geomechanical model, and inclination and azimuth of the well with respect to the pre-dominant direction of polygonal faulting. These parameters were weighed (admittedly, quite a subjective process) and used in an algorithm to calculate "Risk of well failure", which is a proxy for the chance that the well will fail during the remaining Tyra field life up to 2042 (see Fig. 18a).

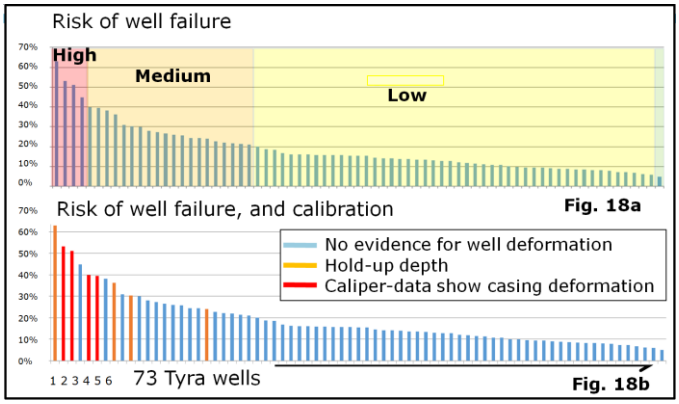

Fig.18. Risk of well failure over remaining Tyra field life composed by blending risk factors from the geomechanical models and Tyra field data (Fig. 18a), and calibration to the actual observations to date on reservoir-compaction-induced damage to Tyra wells in the overburden (Fig. 18b).

The risk rating was then compared to the actual risk status of the 73 Tyra wells, based on well observations during e.g. work-overs and production data. Although this calibration dataset is far from complete, and knowing that we have front-loaded the risking model with observations of caliper data and HUD data (and we can thus expect that this deformation will continue), the well-failure risking model is robust in the sense that 7 out of the 10 wells predicted to be most susceptible to well failure actually show caliper strains and HUDs in the field (see Figure 18b). This calibration gives some confidence that the model will be of use to predict what will happen to these and other wells in the remaining 25 years of the Tyra field life, from 2017 to 2042 (Step 2).

4.3 Impact of well failure on production

In order for the geomechanical "Risk of well failure" tool to be of use, it had to predict the timing of well failure too. Therefore risk factors shown in Figure 18 were scaled with remaining reservoir-life time, and used as input in Monte Carlo simulations to predict timing of well failure. This captures the uncertainty in overburden well failure on the Tyra gas production on ultimate recovery, see Figure 19a, showing *one realization* of timing of well failure for the 73 Tyra wells. Note that the wells in the left part of the graph (which are the ones with the highest risk of shear failure, see Figure 18) generally fail earlier than the low-risk wells to the right of the Figure. However, some of these high-risk wells survive, while some of the low-risk wells fail. By repeating this well-failure-risking many times, a cumulative distribution function is obtained from which the impact of well failure on production can be estimated (Figure 19b).

Depending on the way production and terminal well failure were coupled, the probability of well-failure-induced reduction in production from Tyra Main was calculated. Our first analyses indicate, roughly, a 10% chance of a 5% loss in production due to overburden well failure. At unlikely (1% chance) worst-case conditions of pre-production stress state, stress path and rock and fault properties, there may be a 10% loss of production due to overburden well failure. This production-loss due to geomechanical well failure was smaller than was assumed before the present study was done. It was included in the overall assessment of risk for the Tyra Future project, aimed at adapting the facilities to the subsiding sea-bed to safe-guard the Tyra production for the coming decades.

One of the key learning's from the GEOMEC modeling work is that prediction of shear failure due to reservoir compaction is difficult-if-not-impossible if 1) the pre-production stress state is not known, 2) there is a large uncertainty in mechanical rock properties of faults and country rock (the rock between the faults) and 3) there is insufficient well failure data to calibrate the geomechanical model. Yet, based on our geomechanical modeling work, we consider the risk of any further compaction-induced well failure in the Tyra overburden as **low**, because:

(i) Even in the in-situ stress model with relatively high total stress anisotropy (stress model 2 in Table 1), the faults identified on seismic and the rock between the faults was not at shear failure, and in most cases quite far-away from shear failure (low SCU-values in the Mohr Coulomb stress plot, see Figure 5)

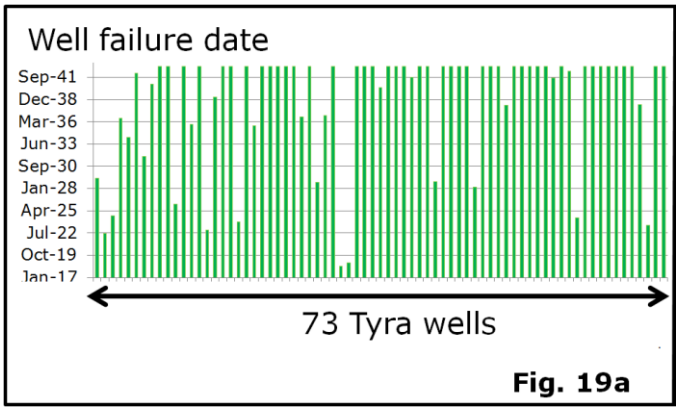

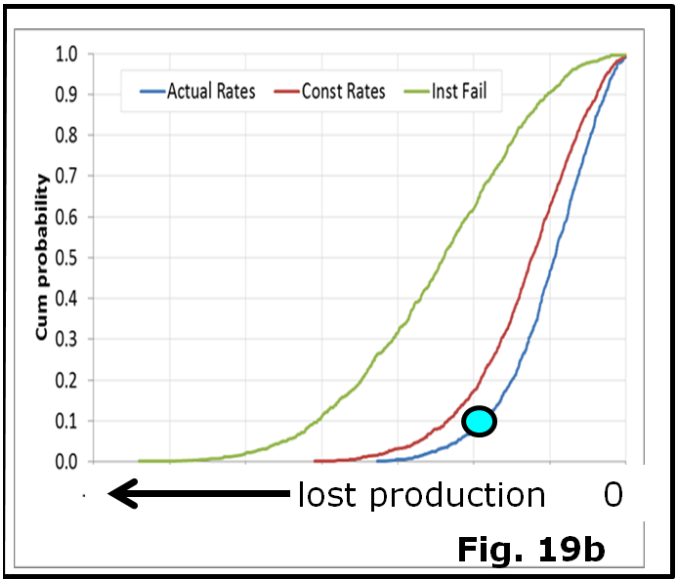

Fig.19. Fig 19a is an example of a Monte Carlo simulation. The green vertical bars show the prediction of timing of terminal well failure for this specific run. Fig. 19b is cumulative distribution function for risk of loss of Tyra production due to well failure. The three curves in Fig. 19b indicate ways in which the well production rates were modeled: red = constant well production rate, blue = well-production decline assumption, green = failure in 2021 for all wells that are predicted to fail from 2016 to 2042 (worst-case). The blue dot is an examples of an assessment of a 10% risk (Y-axis) of a given production loss (X-axis, data not shown for confidentiality reasons).

(ii) The compaction-induced changes in total stress are very small (typically < 5% of the absolute value of the total stress),

(iii) Most of the depletion-induced compaction has already taken place, i.e. the high-porosity Tyra carbonate reservoir probably has already undergone very high compaction strains (5% to 12% strain), and porosity reductions of several porosity units. From a rock physics viewpoint, and as shown by the high seabed subsidence values, it is unlikely that the Tyra reservoir rock will continue to show an increasing compressibility per unit increase in vertical effective stress e.g. due to some kind of a second pore collapse. On the contrary, based on observations in other fields and in laboratory deformation experiments on core, it is likely that the Tyra reservoir rock is already showing a decreasing compressibility with increasing vertical effective stress (compaction hardening, see Figure 2). Since vertical reservoir compaction, overburden deformation and risk of well failure are related mechanically, a reducing reservoir compaction (per unit additional depletion) implies a reducing incremental risk of well failure (per unit depletion) with ongoing depletion.

(iv) The incremental pore pressure depletion in Step 2 is small (about 35% of total compared to pore pressure depletion due to historical production (65% of total in Step 1).

5. CONCLUSIONS

The geomechanical problem/question of reservoir-compaction-induced well failure was investigated and applied to support a business decision in a virtual team of some 15 staff in three companies over 5 locations. It is concluded that:

- the multi-scale geomechanical models indicates that the Tyra reservoir-compaction-induced deformation, displacements and total stress changes in the reservoir are large, and in overburden these are probably small
- well-scale simulations show that cm-size fault slip can strongly deform the casing, *even* if the well is properly cemented. Our geomechanical simulations visually resemble the in-well observations of the geometry of such damage (compare Figure 15 with Figs 1c,d), confirming the localized high-shear-strain (10s of percent) in the casing. So, the 12 observed casing deformations in the Tyra overburden almost certainly have a geomechanical cause
- mechanical-property contrast and/or steep faults could lead to local increases in shear stress and shear stress, notably at the edge of the reservoir. These could produce several cm's of fault slip, which can deform casing *even* if the well is properly cemented.
- Wells intersecting faults at angles of 110° to 150° and (to a lesser extent) 30° to 70° are the most vulnerable in terms of shear-failure-induced well damage
- reservoir well-failure-risking models indicate that 4 to 16 Tyra wells may fail (i.e. seriously hampering or even preventing production) but that the impact on production is probably limited to few percent,
- The risk of compaction-induced terminal well failure from present-day till end of field life in the Tyra reservoir and its overburden is low,
- Overburden well-failure risking models based on full-field and well-scale geomechanics simulations were used to determine which Tyra wells are more vulnerable to shear-slip-induced casing damage than other Tyra wells. Our first analyses indicate, roughly, a 10% chance of a 5% loss in production due to overburden well failure. At unlikely (1% chance) worst-case conditions, there may be a 10% loss of production.

Taking the model and field observations together, our integrated study confirms that the damage to 12 Tyra wells in the overburden has a geomechanical cause. However, based on our geomechanical modeling work and Tyra well-failure measurements collected so far, we consider the risk of further compaction-induced well failure in the Tyra reservoir overburden as **low**, because the geomechanical model indicates that the high-porosity Tyra carbonate reservoir has already undergone very high compaction strains (5% to 12% strain) and porosity reductions of several porosity units. Based on core deformation experiments, it is likely that compaction-hardening has already started in many parts of the reservoir, that is, a decreasing compressibility with increasing vertical effective stress. This will limit vertical compaction and thus reduce the overburden deformation occurring over the next decades of Tyra.

In summary, Tyra wells will continue to be loaded and will deform and fail by the remaining depletion, and well failure risk will increase with further depletion. But the rate at which this risk will increase as a function of depletion will most likely go down with increasing depletion.

ACKNOWLEDGEMENTS

Shell International Exploration and Production B.V and Mærsk Oil, a company of TOTAL, and its Tyra partners are thanked for their guidance to the project and for their permission to present and publish this paper. We thank Nicolas Jensen-Visser, Mark Davison, Alice Post, Raphic van der Weiden, Diederik Wawoe and Marijke Bos and for their technical advice and support.

REFERENCES

1. Abou-Sayed, A.S., F. Meng, J.E. Noble and Q. Guo. 2003. Modeling of reservoir compaction and casing integrity evaluation using reservoir simulation. *SPE* 81072.

2. Bourgeois, F. et al. (2018) Well damage induced by compaction and impact on production on a chalk field. Abstract submitted to EAGE conference, Copenhagen, Denmark, June 2018

3. Bruno, M.S. 2002. Geomechanical and decision analyses for mitigating compaction-related casing damage. SPE Drilling and Completion Jl., p. 179 to 188. *SPE* 79519.

4. Bruno, M.S. 1992. Subsidence-Induced well failure. SPE 20058.

5. Calvert, M.A., A.J. Cherrett, U. Micksch, F.G. Bourgeois and A.S. Calvert (2018). New time lapse seismic attribute linking 4D and geomechanics. Paper accepted at EAGE Conference, Copenhagen, Denmark, June 2018

6. Chernocky, E.P., and E.O. Scholibo. 1995. Approach to casing design for service in compacting reservoirs. *SPE* 30522.

7. Crook, A. J. L., Yu, J. G., Flatebø, R.E. and Kristiansen, T. G. (2008) Computational modeling of the rate dependent deformation and liquefaction of chalk. Paper presented at ARMA 2008 conference

8. De Silva, F.V., G.F. Debande, C.A. Cereira, B. Plischke. 1990. Casing collapse analysis associated with reservoir compaction and overburden subsidence. *SPE* 20953.

9. Dudley, J.W., A. v.d. Linden and G.F. Mueller. 2005. Geomechanical modeling of a pore collapsing carbonate: Compaction and subsidence of a field in Oman, IPTC 10680, *Proceedings of the International Petroleum Technology Conference, Doha, Qatar, 21-23 November*.

10. Dusseault, M.B., M.S. Bruno and J. Barrera. 2001. Casing shear: causes, cases, cures. *SPE* 72060.

11. Furui, K., G.F. Fuh and N. Morita. 2012. Casing-and Screen-Failure analysis in highly compacting sandstone fields. *SPE* 146231.

12. Keszthelyi, D., D.K. Dysthe and B. Jamtveit. 2016. Compaction of North-Sea chalk by pore-failure and pressure solution in a producing reservoir. *Front. Phys.*, 16 Feb. 2016.

13. Khalmanova, D., J.W. Dudley and E.K. Oden. 2008. Geomechanical modeling of subsidence and compaction in the M1 and Jintan gas fields, offshore Malaysia, ARMA 08-192, *Proceedings of the 42nd U.S. Rock Mechanics Symposium, June 29 – July 2, San Francisco, CA.*

14. Kristiansen, T.G., O. Barkved and P.D. Pattillo. 2000. Use of Passive seismic monitoring in well and casing design in the compacting and subsiding Valhall Field, North Sea. *SPE* 65134.

15. Li, X.Q., T.G. Zhu, L.T. Fang and Y. Yuan. 2007. Effect of sand production on casing integrity. *Journal of Canadian Petroleum Technology*. Vol. 46, No. 12.

16. Nagel, N. 2001. Compaction and subsidence issues within the petroleum industry: From Wilmington to Ekofisk and beyond. *Physics and Chemistry of the Earth, Part A: Solid Earth and Geodesy*. Vol. 26, Issues 1–2, 2001, Pages 3-14.

17. Omdal, E., M.V. Madland, T.G. Kristiansen, N.B. Nagel, R.I. Korsnes and A. Hiorth. 2010. Deformation behavior of chalk studied close to in situ reservoir conditions. *Rock Mechanics and Rock Engineering*. Vol. 43, Issue 5, pp.557-580.

18. Peng, S., J. Fu, and J. Zhang. 2007. Borehole casing failure analysis in unconsolidated formations: A case study. *Journal of Petroleum Science & Engineering*.

19. Rhett, D.W. 1998. Ekosfisk Revisited: A new model of Ekofisk reservoir geomechanical behaviour. *SPE* 47273-MS.

20. Teufel, L.W., D.W. Rhett and H.E. Farrell. 1991. Effect of reservoir depletion and pore pressure drawdown on in situ stress and deformation in Ekofisk field, North Sea. Roegiers (ed.). In *Rock Mechanics as Multidisciplinary Science*, Balkema, p. 63-72.

21. Vudovich, A., L.Y. Chin and D.R. Morgan. 1989. Casing deformation in Ekofisk. SPE 17856.

22. Yuan, R.S., Schutjens, P.M.T.M., Bourgeois, F.G. and Calvert, M.A. (2018) Fault slip or bed-parallel shear? – A multi-scenario modeling approach to investigating well deformation in the deep overburden of a compacting reservoir in the North Sea. Paper to be presented at ARMA 2018 conference

23. Zoback, M. and J. Zinke. 2002. Production-induced normal faulting in the Valhall and Ekofisk oil fields. *Pure and Applied geophysics*. Vol. 159, p. 403 to 420.

APPENDIX 1: MODEL OBSERVATIONS WELL-SCALE DEFORMATION CHALK, CEMENT AND CASING

Regarding the **chalk deformation** around the wells (see Figure 20) in all simulations except the two showing divergence, the reservoir developed vertical strains of about 15% (green colors). However, the local deformation of the chalk is affected by the presence of the well. In the near-vertical well (inclination of 10°), the good-cement and partial-cement cases show relatively small vertical strains at the position of the casing collar (red colors) and relatively high vertical strains just below the collar, at the downside of the well. Clearly, the presence of the relatively stiff collar exerts control on the vertical strain around the top of the modeled section of the well. This casing-collar effect is even stronger in the good-cement and partial-cement

wells inclined at 45°, and even two high strain locations can be detected in the partial-cement case. Interestingly, in the good-cement and partial-cement wells inclined at 80° (near-horizontal wells), the casing-collar effect on the vertical strains has disappeared. Furthermore, in the direction orthogonal to the wellbore cylindrical axis, a strong increase in vertical strain (compared to the "background strain" of 0.15) is shown of up to 0.31 (blue colors), but with a narrow zone, oriented parallel to the well axis extending horizontally away from it, of very low vertical strain of about 0.02 (red colors). This narrow low-strain zone is probably "protected" from undergoing the high compaction strain by the presence of the relatively stiff casing, while the two zones just above and below it deform more as a result of load transfer around the near-horizontal casing. In the near-horizontal well with patchy cement, another relatively-low-strain zone appears at the bottom of the well, at the location of the poor-cement section. In the poor-cement well that is oriented near-vertically, the casing-collar effect is much smaller than in the near-vertical wells with good and patchy cement. In contrast, the two poor-cement wells with inclinations of 45° and 80° show zones of low strain of about 0.02 above and below the casing, while in the zone parallel to the casing axis and extending horizontally away from it, the background vertical strain is about 15%. Note that these two simulations are for the years 2035 and 2029, where the divergence occurred.

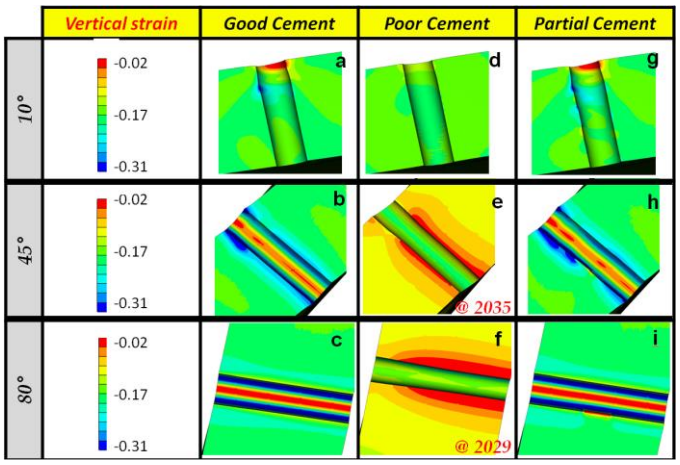

Fig. 20. Modeled vertical strain in the **reservoir chalk** at the end of field life (year 2042) showing the effects of depletion-induced reservoir compaction as a function of well inclination and cementation quality. Simulations with poor-cement at well inclinations of 45° and 80° fail in year 2035 and 2029, respectively, due to divergence to main distortion (i.e. high local deformation).

Regarding the **cement deformation**, Figure 21 shows the plastic strains in the cement. (Note that the reservoir strains are grayed-out, to enable better comparison between the model results of these nine simulations.) Starting with the near-vertical well (inclination 10°), the two cases with good cement and partial-cement indicate that the presence of the mechanically stiff casing collar (compared to the "normal-strength" casing above and below it) also has an effect on the strain in the cement: At the location of the casing collar, the plastic strain is relatively low and in the cement just below the casing collar, the plastic strain is relatively high, reaching values of 0.5. In both simulations, the cement in the rest of the casing undergoes similar plastic strains as the chalk. The situation is very different in the 10°-inclination poor-cement well, where very high plastic strains develop in the cement along its entire length. This is not surprising perhaps, given its relatively low strength compared to the cement quality used in the good-cement and partial-cement simulations. Yet, of key importance here is that, although the poor-quality cement shows a high degree of deformation, the simulation is able to run till the full far-field vertical uniaxial strain of 0.15 is applied. That is, even though the cement shows very high plastic strain, and can thus be considered as "failed" in a mechanical sense, the well still has strength and has not "failed" in the sense of causing an ultra-high strain or stress-change that causes the computer model to diverge ("crash"). Inclining the wells from 10° to 45° shows significantly lower plastic strains in the cement in the 45°-inclination wells than in the 10°-inclination wells.

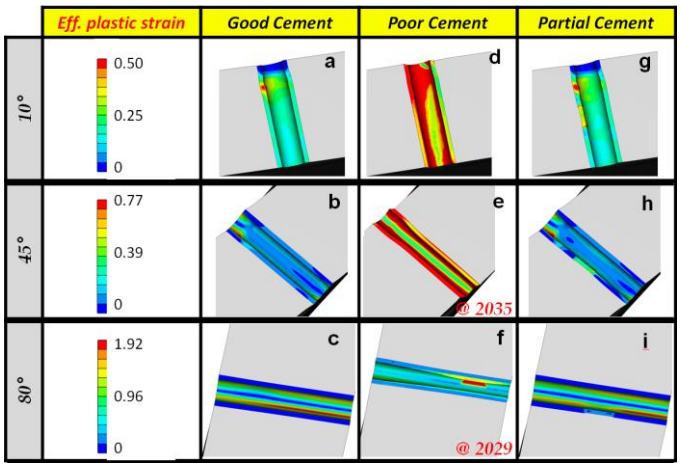

Fig. 21. Modeled plastic strain (Von Mises strain) in the **cement** at end of field life, year 2042. All results are for year 2042, except for the poor-cement 45°-inclination and for the poor-cement 80°-inclination well. The results from these two simulations are from years 2035 and 2029, respectively, when the model became numerical unstable due to local casing collapse by strong ovalization.

The effect of the casing collar on the cement strain is still visible in these two wells, but it is much less pronounced than in the 10°-inclination wells. There are large variations in cement strain along the well, notably in the 45°-inclination partial-cement simulation. Interestingly, although similar high plastic strains develop in the poor-cement 45°-inclination wells as in the poor-cement 10°-inclination well, the poor-cement

45°-inclination wells "fails" in the computer-year 2035 (as indicated by the divergence) while the poor-cement 10°-inclination well appears to maintain its mechanical integrity throughout its field life. The simulation of the deformation in the near-horizontal (80°-inclination) wells with good cement and partial cement again show the alternation of low and high plastic strains that are also visible in the chalk. Starting from values of near-zero plastic strain at the top and bottom part of the cement surrounding the casing, the plastic strains increase to very high values of 1 in the top part and 2 in the lower part of the cement. At the sides of the well, i.e. alongside the cylindrical axis of the well, a low-strain zone is visible. In the near-horizontal (80°-inclination) well with poor cement, strains in 2029 are in the range 0.5 to 1.0, but with a zone of very-high plastic strain of 1.5 to 2 in the lower part of the well. This is the ovalization development (that also led to the divergence of the computer model calculations) that is thus clearly related to the poor-cement unable to "protect" the near-horizontal well from collapsing as the far-field strain of 0.15 is applied. Key points on cement deformation are:

- at all three inclinations, the poor cement fails extensively.
- the good and partial cement show localized plastic strain where
- wrinkling is occurring on downside of well, immediately beneath collar (10° and 45°);
- in vicinity of partial/poor-cement pocket (10° and 45°);
- along inner cement – casing interface (80°).

Regarding the **casing deformation** (Figure 22), the key results can be summarized as follows:

- at inclinations of 10° and 45°, the good and partial cases exhibit localized high plastic strain immediately below the casing collar (wrinkling) while the poor cement cases do not (load not transferred onto casing due to extensive shearing of cement),
- secondary localisations are located in the vicinity of the partial poor cement pocket inclinations of 10° and 45°,
- the 80°-cases exhibit a band of high plastic strain along the inner diameter, at the axis of minimum diameter increase due to ovalization. This band is more extensive and also affects the collar in the poor cement case.
- the results for the poor-cement 45°-inclination and poor-cement 80°-inclination well are for the years 2035 and 2029, respectively, when the model became numerical unstable due to local casing collapse by strong ovalization.
- Figure 23 shows plastic strain in the steel casing at year 2029, which is the year when the 80°-inclination well failed.

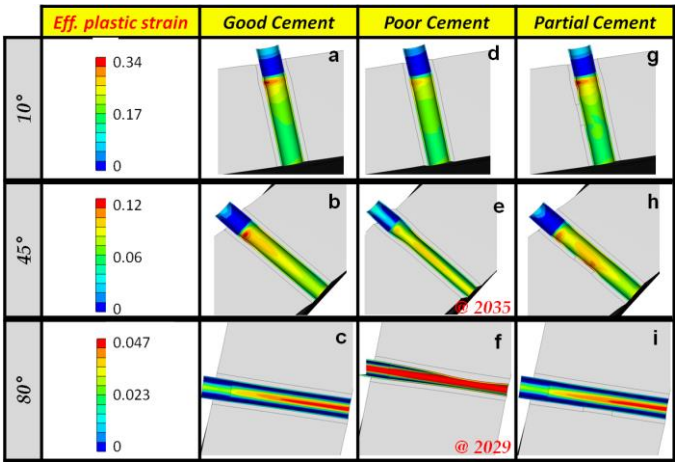

Fig. 22. Modeled plastic strain in **steel casing.** All results are for 2042, except poor-cement 45°-inclination and poor-cement 80°-inclination well for the years 2035 and 2029, respectively, when the model became numerical unstable due to local casing collapse by strong ovalization.

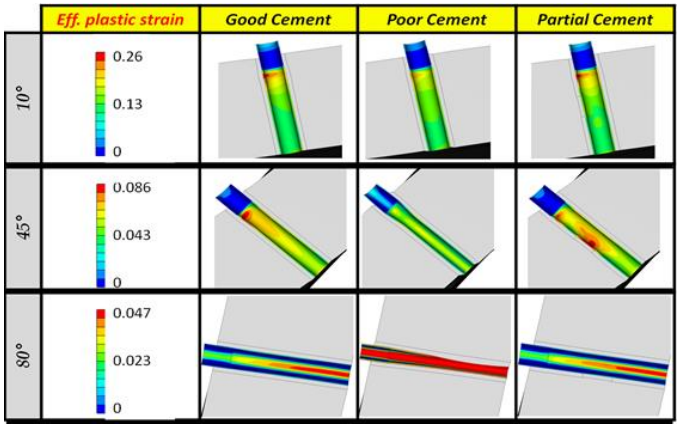

Fig. 23. Modeled plastic strain in the ***steel casing*** at year 2029, which is the year when the 80°-inclination well failed.

APPENDIX 2 DEFINITION OF PLASTIC STRAIN

Incremental effective plastic strain (called Von Mises strain in this paper) is defined as

$$\overline{d\varepsilon^p} = \sqrt{\frac{2}{3}\left[(d\varepsilon_x^p - d\varepsilon_v^p)^2 + (d\varepsilon_y^p - d\varepsilon_v^p)^2 + (d\varepsilon_z^p - d\varepsilon_v^p)^2 + \frac{1}{2}\left(d\gamma_{xy}^{p\,2} + d\gamma_{yz}^{p\,2} + d\gamma_{xz}^{p\,2}\right)\right]}$$

or, in tensor form

$$\overline{d\varepsilon^p} = \sqrt{\frac{2}{3}\sqrt{d\varepsilon_{ij}^{p\prime} d\varepsilon_{ij}^{p\prime}}}$$

where

$$d\varepsilon_{ij}^{p\prime} = \begin{cases} d\varepsilon_{ij}^p - d\varepsilon^v & i = j \\ d\varepsilon_{ij}^p & i \neq j \end{cases}$$